Materials & Design 265 (2026) 115766

Contents lists available at ScienceDirect

Materials & Design

journal homepage: www.elsevier.com/locate/matdes

A physics-informed coupled residual-Fourier neural network for multi-physics field prediction in laser manufacturing

Wenbo Zhou[a,d], Le Song[b], Xuyang Chen[a,c,*], Zhiyong Huang[b], Baorui Du[a]

[a] Institute of Engineering Thermophysics, Chinese Academy of Sciences, 100190, Beijing, China
[b] School of Computing, National University of Singapore, Singapore, 117576, Singapore
[c] Institute of Applied Materials – Microstructure Modelling and Simulation, Karlsruhe Institute of Technology, Karlsruhe, Germany
[d] Institute of Systems Science, National University of Singapore, Singapore, 119615, Singapore

HIGHLIGHTS

- A stepwise training strategy is proposed for coupled multi-physics fields.
- Temperature-concentration and velocity fields are trained sequentially to improve stability.
- The method achieves about 5.73x speedup over conventional numerical simulations.
- The trained model predicts refined grids in seconds without re-simulation via interpolation.

GRAPHICAL ABSTRACT

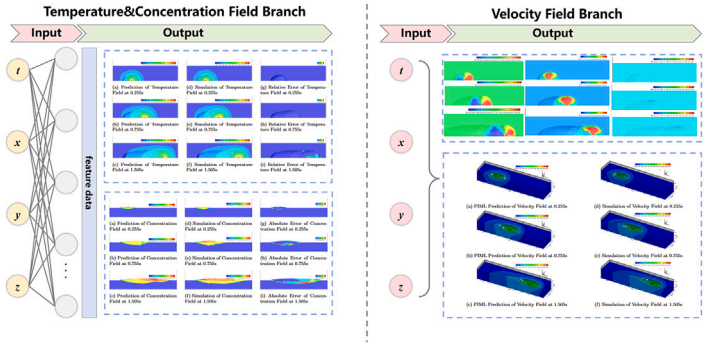

ARTICLE INFO

Keywords:
Physics-informed machine learning
Melting pool prediction
Fourier neural network
Multi-physics prediction
Hybrid laser-MIG welding

ABSTRACT

In hybrid laser-MIG(Metal Inert Gas) welding, multi-physics field prediction in the melting pool is crucial for process optimization and quality control. However, the complex coupling among temperature, concentration, and velocity fields makes conventional simulations computationally expensive. This paper presents a Physics-Informed Coupled Residual-Fourier Network (PCRF-Net) method for multi-physics field prediction in the melting pool using simulation data and coupling physical residual equations. The method consists of a dual-branch architecture: the temperature and concentration fields branch uses deep residual networks, integrating energy conservation and solute transport equation residuals to predict the temperature field and concentration distribution; the velocity field branch employs a Fourier-enhanced multilayer perceptron to predict velocity fields that capture long-range flow structures, while applying a temperature mask to restrict training to the molten regions. A stepwise training strategy is adopted, where the TC-Branch is trained first, and then the trained temperature field is used to guide the VF-Branch training, effectively reducing the complexity of multi-physics coupling. Compared to numerical simulation results, the method efficiently learns the temperature, concentration, and velocity fields generated by the coupling of laser and MIG heat sources, achieving second-level fast prediction. This demonstrates its great potential for real-time monitoring and parameter optimization in hybrid laser-MIG welding processes.

* Corresponding author at: Institute of Engineering Thermophysics, Chinese Academy of Sciences, 100190, Beijing, China.
Email address: chenxy.2018@tsinghua.org.cn (X. Chen).

https://doi.org/10.1016/j.matdes.2026.115766
Received 1 December 2025; Received in revised form 12 January 2026; Accepted 1 March 2026
Available online 10 March 2026

1. Introduction

Laser-MIG Hybrid Welding is a highly coupled multi-scale, multi-physics process [1]. Direct experimental observation of the temperature and flow within the melt pool requires expensive equipment and complex operations, limiting process optimization [2]. Traditional numerical simulation methods (such as the finite element method, and finite volume method) predict the formation and characteristics of the melt pool through mathematical models, and have made progress in the study of solidification processes and solute transport [3]. However, heat conduction and flow in the melt pool are significantly coupled, with liquid metal convection typically being the main mode of heat transfer in the weld pool, determining the temperature distribution and weld shape. The liquid flow is driven by multiple forces, including surface tension gradients, electromagnetic forces, and buoyancy [4]. To obtain accurate 3D results, finite element models require fine meshes and consideration of complex boundary conditions, leading to huge computational costs [5]. For instance, Zhou et al. [6] developed a mathematical model to study the complex transport phenomena in point-based hybrid laser-MIG keyhole welding. Jiang et al. [7] developed a multi-physics model to study the solidification process in 5083 aluminum alloy laser welding. Qing et al. [8] developed a multi-scale model to simulate the molten deposition process in 3D printing. However, traditional numerical methods require a significant amount of time and high-performance computing frameworks to solve complex multi-scale, multi-physics models, which cannot meet industrial demands [9].

The development of Artificial Intelligence has provided new ideas for welding process modeling. Physics-Informed Neural Networks (PINNs) solve scientific problems with minimal data by embedding the residuals of partial differential equations into the loss function [10]. For example, Zhu et al. [9] proposed a transfer learning-enhanced physics-informed neural network (TLE-PINN) to improve melt pool prediction in selective laser melting, integrating EPINN and transfer learning to enhance training speed and accuracy. Seid et al. [11] applied the PINN model to solve the heat conduction equation, providing a new computational framework that can reliably and quickly predict results after sufficient training. Li et al. [12] developed a PINN model to predict the temperature field in the laser metal deposition process without requiring labeled data. Wang et al. [13] proposed a physics-informed machine learning method connecting relevant parameters in selective laser melting, effectively predicting quality characteristics. Akbari et al. [14] developed a physics-aware machine learning method to predict melt pool shapes and geometries in metal additive manufacturing.

However, most of these methods can only solve single-physics problems, and there is less focus on the prediction of 3D concentration and velocity fields [15]. Many existing studies using PINN solve simple equations, but challenges remain when facing complex multi-physics coupled problems, especially when dealing with multiple coupled equations [16]. Moreover, PINNs involving multiple coupled equations require the simultaneous optimization of multiple physical residuals, and the loss function becomes a complex non-convex multi-objective form, making the training process unstable [17].

To more efficiently predict multi-physics fields in hybrid laser-MIG welding melt pools, this paper proposes a Physics-Informed Coupled Residual-Fourier Network (PCRF-Net) method. This method uses numerical simulation data as training samples and incorporates physical residuals into the loss function, combining deep residual learning and Fourier operations to capture complex coupling features. Specifically:

- **Temperature-Concentration Branch (TC-Branch)**: A deep residual network is used to predict the temperature and concentration distributions. The residual network simplifies the training of deep networks by introducing residual connections, allowing it to effectively learn complex mappings. Energy conservation and solute transport equation residuals are added to the loss function, ensuring that the network adheres to the laws of heat conduction and solute diffusion while fitting the numerical data.
- **Velocity Field Branch (VF-Branch)**: A Fourier-augmented multilayer perceptron is used to predict velocity components. By applying a real-valued Fast Fourier Transform to the input spatial-temporal coordinates, global low-frequency amplitude features are extracted, which are combined with time-domain projections to efficiently represent long-range flow structures driven by surface tension, electromagnetic forces, and buoyancy. Fourier transforms provide the network with a non-local receptive field, capturing global features that conventional convolutions cannot. A temperature mask is used to backpropagate gradients in the molten region, in accordance with phase change physics.
- **Stepwise Training Strategy**: Unlike traditional PINNs that embed all physical equations simultaneously, PCRF-Net first trains the TC-Branch to obtain stable temperature and concentration predictions. Then, the predicted temperature field is used to identify the molten region and guide the VF-Branch's training in the effective region. Similar to stress splitting sequential training methods, this stepwise strategy reduces the rigidity of multi-objective losses and improves training stability.
- **Experimental Verification**: To validate the PCRF-Net method, it is first compared with traditional numerical simulation methods. By comparing the melt pool cloud images, the results show that PCRF-Net's predictions of the temperature, concentration, and velocity fields align well with traditional numerical simulation models. Since experiments cannot directly measure all physical field parameters, especially the velocity field [18], the velocity fields' validation can only be done by comparing cloud images with simulation results. Therefore, the accuracy of the PCRF-Net model can be indirectly validated by comparing the predicted results with experimental data on melt pool dimensions such as melt width, melt height, melt depth, and concentration distribution.

This method effectively combines physical equations and numerical simulation data, enhancing the model's physical consistency and training efficiency. By decomposing the training of the TC-Branch and VF-Branch, the model better handles features at different scales, avoiding training instability caused by scale differences. After training, the model can predict different grid resolutions for the same operating conditions in seconds through interpolation methods.

2. Mathematical model

The material of the base metal is A7N01 aluminum alloy, and the material of the filler wire is ER5356 aluminum alloy [19]. The main components of the base metal and filler wire are aluminum, magnesium and zinc, and the content of other elements is quite small. Therefore, the composition of the filler wire is assumed to be 95 percent aluminum and 5 percent magnesium, while the composition of the base metal is assumed to be 95.5 percent aluminum and 4.5 percent zinc, and other elements are neglected. When the base metal begins to melt, the liquid flow in the molten pool is assumed to be Newtonian, incompressible and laminar [20].

Material compositions of A7N01 aluminum and ER5356 welding wire Table 1.

2.1. Governing equations

The nomenclature is provided in Table 2.The continuity, momentum, energy and species equations are used as follows [21–23].

Continuity Equations:

$$\frac{\partial \rho}{\partial t} + \frac{\partial \left(\rho u_i\right)}{\partial x_i} = 0 \tag{1}$$

Table 1
Material compositions of A7N01 aluminum and ER5356 welding wire.

Materials	Mg	Zn	Fe	Mn	Si	Cr	Ti	Cu	Al
A7N01	1.0–2.0	4.0–5.0	0.35	0.2–0.7	<0.30	<0.30	<0.20	<0.20	Bal.
ER5356	4.5–5.5	<0.1	<0.4	0.05–0.2	<0.25	0.05–0.2	0.06–0.2	<0.10	Bal.

Table 2
Nomenclature.

g	Acceleration due to gravity	I	Welding current
t	Time	h_c	Heat transfer coefficient
x_i	Distance along i directions	t_{bx}	Tangential unit vector parallel to the x-z plane
u_j	Liquid velocity along j direction	t_{by}	Tangential unit vector parallel to the y -z plane
P	Pressure	n_b	Outward normal vector
V	Scanning speed	f	Frequency of droplet transfer
f_l	Liquid fraction	ρ_w	Density of welding wire
C_p	Specific heat	C_w	Specific heat capacity of welding wire
ΔH	Latent heat content	d_w	Wire diameter
F	Volume force	U_w	Wire feed speed
F_{Lx}	Electromagnetic force along x direction	T	Temperature
F_{Ly}	Electromagnetic force along y direction	T_w	Droplet temperature
F_{Lz}	Electromagnetic force along z direction	T_l	Liquidus temperature
h	Sensible heat enthalpy	T_{ref}	Reference temperature
k	Thermal conductivity	T_a	Ambient temperature
C	Concentration		
C_l	Concentration in liquid phase	Greek symbols	
C_s	Concentration in solid phase	ρ	Density
C_{ref}	Reference Concentration	μ	Viscosity
D	Diffusion coefficient of element	μ_m	magnetic permeability
Q_{laser}	Body heat source of laser	β	Coefficient of volume expansion
Q_{arc}	Body heat source of arc	γ	Surface tension
Q_d	Sensible heat from droplets	$\frac{d\gamma}{dT}$	Temperature coefficient of surface tension
q_{laser}	Surface heat source of laser	σ	Stefan-boltzmann constant
r	Radius	σ_j	Radius of the arc pressure
H	Thickness of workpiece	ε	Surface emissivity
L	Characteristic length		

Momentum Equations:

$$\frac{\partial\left(\rho u_j\right)}{\partial t}+\frac{\partial\left(\rho u_i u_j\right)}{\partial x_i}=\frac{\partial}{\partial x_i}\left(\mu\frac{\partial u_j}{\partial x_i}\right)+\left(-\frac{\partial P}{\partial x_i}\right)+\frac{\partial}{\partial x_j}\left(\mu\frac{\partial u_j}{\partial x_i}\right)-V\frac{\partial\left(\rho u_i\right)}{\partial x}-C\left(\frac{\left(1-f_l\right)^2}{f_l^3+B}\right)u_i+F \tag{2}$$

Energy Equations:

$$\frac{\partial(\rho h)}{\partial t}+\frac{\partial\left(\rho u_i h\right)}{\partial x_i}=\frac{\partial}{\partial x_i}\left(\frac{k}{C_p}\frac{\partial h}{\partial x_i}\right)-\frac{\partial(\rho\Delta H)}{\partial t}-\frac{\partial\left(\rho u_i\Delta H\right)}{\partial x_i}-V\frac{\partial(\rho h)}{\partial x}-V\frac{\partial(\rho\Delta H)}{\partial x}+Q_{\text{laser}} \tag{3}$$

Species Equation:

$$\frac{\partial(\rho C)}{\partial t}+\frac{\partial\left(\rho u_i C\right)}{\partial x_i}=\frac{\partial}{\partial x_i}\left(\rho D\frac{\partial C}{\partial x_i}\right)+\frac{\partial}{\partial x_i}\left(\rho D\frac{\partial\left(C_l-C\right)}{\partial x_i}\right)-\frac{\partial}{\partial x_i}\left(\rho f_s\left(C_l-C_s\right)u_i\right) \tag{4}$$

The porous media term on the right-hand side of Eq. (2) was represented based on the Carman-Kozeny equation. F is the volume force, including electromagnetic force and buoyancy caused by concentration and temperature variations. The electromagnetic force can be expressed as:

$$F_{Lx}=-\frac{\mu_m I^2}{4\pi^2\sigma_j^2 r}\exp\left(-\frac{r^2}{2\sigma_j^2}\right)\left[1-\exp\left(-\frac{r^2}{2\sigma_j^2}\right)\right]\left(1-\frac{z}{H}\right)^2\frac{x}{r} \tag{5}$$

$$F_{Ly}=-\frac{\mu_m I^2}{4\pi^2\sigma_j^2 r}\exp\left(-\frac{r^2}{2\sigma_j^2}\right)\left[1-\exp\left(-\frac{r^2}{2\sigma_j^2}\right)\right]\left(1-\frac{z}{H}\right)^2\frac{y}{r} \tag{6}$$

$$F_{Lz}=-\frac{\mu_m I^2}{4\pi^2\sigma_j^2 r}\exp\left(-\frac{r^2}{2\sigma_j^2}\right)\left[1-\exp\left(-\frac{r^2}{2\sigma_j^2}\right)\right]\left(1-\frac{z}{H}\right) \tag{7}$$

The expression for buoyancy is as follows:

$$F_b=\rho g\beta\left(T-T_{\text{ref}}\right)+\rho g\beta\left(C-C_{\text{ref}}\right) \tag{8}$$

The last two terms in Eq. (4) represent the solute partitioning at the liquid-solid interface. The formulation of nominal concentration, density, thermal conductivity, heat capacity, and mass diffusion coefficient for the mushy zone can be summarized as follows.

$$C=f_s C_s+f_l C_l \tag{9}$$

$$\rho=f_s\rho_s+f_l\rho_l \tag{10}$$

$$k=\left(\frac{g_s}{k_s}+\frac{g_l}{k_l}\right)^{-1} \tag{11}$$

$$c=f_s c_s+f_l c_l \tag{12}$$

$$D=f_l D_l \tag{13}$$

2.2. Boundary conditions

The boundary condition for energy can be given as

$$-k\nabla T\cdot\boldsymbol{n}_b=q_{\text{laser}}+q_{\text{arc}}+\mathrm{Q_d}(x,y)-\sigma\varepsilon\left(T^4-T_a^4\right)-h_c\left(T-T_a\right) \tag{14}$$

The detailed description of the heat source model of laser and arc, and the free surface evolution of the molten pool can be found in the literature.

Table 3
Material properties.

Property (Unit)	Substrate (A7N01)	Welding wire (ER5356)
Solidus temperature(K)	858	813
Liquidus temperature(K)	923	908
Density of liquid metal (kg/m^3)	2700	2380
Enthalpy of solidus temperature (J/kg)	7.6×10^5	7.4×10^5
Enthalpy of liquidus temperature (J/kg)	1.1×10^6	1.03×10^6
Specific heat of liquid (J/(kg. K))	1200	1135
Specific heat of solid (J/(kg. K))	881	913
Thermal conductivity of liquid ((W/(m · s)))	80	83
Thermal conductivity of solid ((W/(m · s)))	101	108
Effective mass diffusivity (m^2/s)	7^*10^{-7}	$7*10^{-7}$
Temperature coefficient of surface tension (N/(m · K))	-1.55×10^{-4}	-1.7×10^{-4}
Viscosity of liquid ((kg/(m · s)))	1.0×10^{-3}	1.0×10^{-3}

Table 4
Processing parameters.

Parameter (Unit)	Value
Voltage(V)	21.3
Welding current(A)	150
Effective laser radius (mm)	0.15
Wire diameter (mm)	1.2
Droplet temperature(K)	1923
Wire feeding rate (m/min)	9.3
Ambient temperature(K)	298
Radius of droplet impact (mm)	1.0
Distance between MIG torch and laser (mm)	2
Frequency of droplet transition (Hz)	317
Stefan–Boltzmann constant σ (W/(m^2·K^4))	5.670×10^{-8}
Surface emissivity	0.47

The heat distribution of the droplet was approximated as a Gaussian:

$$Q_d(x,y)=\frac{C_w\rho_w\frac{\pi}{4}d_w^2U_w\left(T_w-T_l\right)}{2\pi r_f^2 f}\exp\left(\frac{x^2+y^2}{2r_f^2}\right) \tag{15}$$

The boundary condition for momentum can be expressed as

$$\mu\frac{\partial u}{\partial z}\cdot\boldsymbol{n}_b=f_l\frac{\partial\gamma}{\partial T}\left(\frac{dT}{dx}\cdot\boldsymbol{t}_{bx}\right)+f_l\frac{\partial\gamma}{\partial C}\left(\frac{dC}{dx}\cdot\boldsymbol{t}_{bx}\right) \tag{16}$$

$$\mu\frac{\partial v}{\partial z}\cdot\boldsymbol{n}_b=f_l\frac{\partial\gamma}{\partial T}\left(\frac{dT}{dy}\cdot\boldsymbol{t}_{by}\right)+f_l\frac{\partial\gamma}{\partial C}\left(\frac{dC}{dy}\cdot\boldsymbol{t}_{by}\right) \tag{17}$$

$$w\cdot\boldsymbol{n}_b=0 \tag{18}$$

The Marangoni convection caused by temperature and concentration variations is represented on the right-hand side in Eqs. (16) and (17).

Material properties of the substrate and welding wire are as follows Table 3.

Processing parameters are in Table 4.

3. Proposed method

3.1. PCRF-Net framework and training data

The PCRF-Net architecture is shown in Fig. 1. The training data comes from the computational results of traditional numerical simulations. The 3D high-fidelity coupled model of heat conduction, fluid flow, and solute transport is developed using the Finite Volume Method (FVM) and implemented in FORTRAN. The simulation parameters used in this study have been calibrated by the researchers [21,24] and adjusted based on the consistency between the computational results and experimental data. The adjusted computational results are consistent with the experimental data and can be used as input data for the proposed algorithm. This numerical simulation model does not include turbulence effects and assumes laminar flow, making it suitable for simulating melt pool flow in the hybrid laser-MIG welding process.

Training Data and Grid Discretization: The training data uses a coarse grid with 148 grid points in the x-direction, 34 grid points in the y-direction, and 41 grid points in the z-direction (148×34×41). All grid points are used for training, requiring no additional sampling strategy. For each spatio-temporal coordinate point (x_i, y_j, z_k, t), we have corresponding ground truth labels (temperature T, concentration C, and velocity components u, v, w), which are obtained from numerical simulation results.

Fine Grid Testing and Expected Results: To validate the model's predictive capability and generalization performance at higher resolution, we test using a fine grid (292×66×41). The trained model extends predictions from the coarse grid (148×34×41) to the fine grid (292×66×41) resolution through interpolation methods. Expected results demonstrate that PCRF-Net can maintain high-precision predictions at fine grid resolution while significantly improving computational efficiency. More importantly, after training, the network can predict any refined grid in seconds without requiring additional numerical simulations.

3.1.1. Temperature-concentration branch

This branch employs a lightweight residual multilayer perceptron (ResNet-MLP) structure. The input consists of spatio-temporal coordinates (x, y, z, t), with a hidden layer width of 128 and 34 residual blocks. The network predicts temperature T and concentration C separately, with approximately 227,000 trainable parameters in total.

After scale normalization, the input passes through a linear projection layer with ReLU activation, then sequentially through 34 residual blocks, and finally branches into temperature and concentration output heads. During training, concentration labels are scaled to match the value ranges. The loss function includes data fitting loss and governing equation residual loss. When computing the governing equation residuals, the network outputs T and C are differentiated using automatic differentiation to compute their spatial and temporal derivatives. The velocity terms u_i in the equations use ground truth values from the training data at corresponding spatiotemporal coordinate points, and are detached from the computational graph using gradient clipping methods, such that u_i participates as constants in the residual computation (e.g., in $\frac{\partial(\rho u_i h)}{\partial x_i}$, u_i is treated as a constant and only $h(T)$ is differentiated), but do not participate in the backpropagation of network parameters. This approach ensures the physical completeness of the equations while allowing the TC-Branch to focus on learning the physical relationships of temperature and concentration fields, with the velocity field independently learned by the VF-Branch.

The governing equation residual loss for the TC-Branch consists of the residuals from the energy equation and the species equation. The energy equation residual loss L_{energy} and the species equation residual loss L_{species} are defined by Eqs. (20) and (22), respectively, and their corresponding residual terms R_{energy} and R_{species} are given by Eqs. (19) and (21), respectively. The total governing equation residual loss L_{GE} is the weighted sum of the two, as shown in Eq. (23).

$$\begin{aligned}R_{\text{energy}}=&\frac{\partial(\rho h)}{\partial t}+\frac{\partial(\rho u_i h)}{\partial x_i}-\frac{\partial}{\partial x_i}\left(\frac{k}{C_p}\frac{\partial h}{\partial x_i}\right)+\frac{\partial(\rho\Delta H)}{\partial t}+\frac{\partial(\rho u_i\Delta H)}{\partial x_i}\\&+V\frac{\partial(\rho h)}{\partial x}+V\frac{\partial(\rho\Delta H)}{\partial x}-Q_{\text{laser}}\end{aligned} \tag{19}$$

$$L_{\text{energy}}=\frac{1}{N}\sum_{n=1}^{N}\left|R_{\text{energy}}(x_n,t_n)\right|^2 \tag{20}$$

$$\begin{aligned}R_{\text{species}}=&\frac{\partial(\rho C)}{\partial t}+\frac{\partial(\rho u_i C)}{\partial x_i}-\frac{\partial}{\partial x_i}\left(\rho D\frac{\partial C}{\partial x_i}\right)-\frac{\partial}{\partial x_i}\left(\rho D\frac{\partial(C_l-C)}{\partial x_i}\right)\\&+\frac{\partial}{\partial x_i}\left(\rho f_s(C_l-C_s)u_i\right)\end{aligned} \tag{21}$$

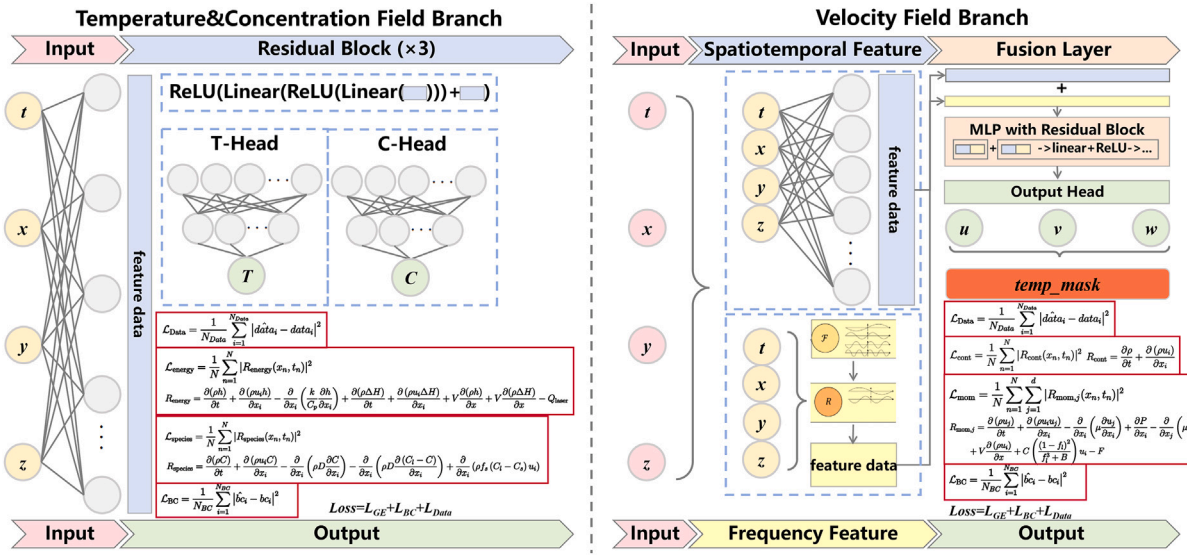

Fig. 1. Framework of TC-Branch & VF-Branch.

$$L_{\text{species}} = \frac{1}{N}\sum_{n=1}^{N} |R_{\text{species}}(x_n, t_n)|^2 \tag{22}$$

$$L_{\text{GE}} = \lambda_1 L_{\text{energy}} + \lambda_2 L_{\text{species}} \tag{23}$$

3.1.2. Velocity field branch

This branch employs a Fourier-MLP structure, which is a Fourier-enhanced PINN architecture. The input consists of spatio-temporal coordinates (x, y, z, t), with a hidden layer width of 256 and 20 Fourier modes (the optimal configuration determined through sensitivity analysis, see Section 4.3.3). The network predicts velocity components and pressure (u, v, w, P) through the fusion of temporal and frequency domain features, with approximately 278,000 trainable parameters in total.

After scale normalization, the input first passes through the temporal projection layer to obtain spatiotemporal features, while simultaneously performing a real-valued fast Fourier transform on the coordinate vector to extract frequency-domain features. The temporal and frequency-domain features are then fused and sequentially passed through 4 Fourier-enhanced layers and a residual projection layer. Finally, the output network predicts three velocity components and pressure (u, v, w, P). Since the spatial distribution pattern of the velocity field is primarily determined by the spatial coordinate distribution of heat sources, the heat source terms $Q_{\text{laser}}(x, y, z)$ and $Q_{\text{arc}}(x, y, z)$ are functions of spatial coordinates, applying Fourier transform to coordinates can effectively capture long-range spatial information, helping the network understand the formation mechanism of the velocity field. Experimental validation (see Table 9) shows that this design improves prediction accuracy by 8.2% in terms of Peclet number (Pe) prediction compared to standard PINN (R^2 increases from 0.8063 to 0.8727).

Additionally, as the numerical simulation data lack the ground truth of the pressure field, the pressure field is learned indirectly through the momentum equation residual loss without evaluation.

To match the phase transition physical characteristics, a dynamic temperature mask is constructed during training based on the temperature field predicted by the TC branch, and velocity component losses are calculated and backpropagated only in the molten or mushy regions. This strategy is based on two reasons: (1) Physical rationality: Materials in unmelted regions are in a solid state, where no fluid flow exists and the velocity field should be zero. Therefore, training the velocity field in unmelted regions has no physical significance. (2) Training efficiency: Training only in meaningful regions (molten regions) can reduce ineffective computations and improve training efficiency. The loss function includes data fitting loss and governing equation residual loss. When computing the governing equation residuals, the network outputs u, v, and w compute their spatial and temporal derivatives through automatic differentiation. The temperature and concentration related terms in the equations use the predicted values $T_{\text{pred}}(x, y, z, t)$ and $C_{\text{pred}}(x, y, z, t)$ from the trained TC-Branch at corresponding spatiotemporal coordinates. These predicted values are functions of spatiotemporal coordinates, thus they can be differentiated with respect to coordinates to compute the related terms in the physical equations. However, the gradient clipping method disconnects T_{pred} and C_{pred} from the computational graph of the VF-Branch network parameters, preventing them from participating in the backpropagation of the VF-Branch network parameters. This design allows the VF-Branch to leverage the predictions from the TC-Branch, demonstrating the advantages of the step-by-step training strategy, while ensuring the physical completeness of the equations and the VF-Branch's focus on learning the physical relationships of the velocity field.

The governing equation residual loss for the VF-Branch consists of the residuals from the continuity equation and the momentum equation. The continuity equation residual loss L_{cont} and the momentum equation residual loss L_{mom} are defined by Eqs. (25) and (27), respectively, and their corresponding residual terms R_{cont} and R_{mom} are given by Eqs. (24) and (26), respectively. The total governing equation residual loss L_{GE} is the weighted sum of the two, as shown in Eq. (28).

$$R_{\text{cont}} = \frac{\partial \rho}{\partial t} + \frac{\partial(\rho u_i)}{\partial x_i} \tag{24}$$

$$L_{\text{cont}} = \frac{1}{N}\sum_{n=1}^{N} |R_{\text{cont}}(x_n, t_n)|^2 \tag{25}$$

$$R_{\text{mom},j} = \frac{\partial(\rho u_j)}{\partial t} + \frac{\partial(\rho u_i u_j)}{\partial x_i} - \frac{\partial}{\partial x_i}\left(\mu \frac{\partial u_j}{\partial x_i}\right) + \frac{\partial P}{\partial x_i} - \frac{\partial}{\partial x_j}\left(\mu \frac{\partial u_j}{\partial x_i}\right) + V\frac{\partial(\rho u_i)}{\partial x} + C\left(\frac{(1-f_l)^2}{f_l^3 + B}\right)u_i - F \tag{26}$$

$$L_{\text{mom},j} = \frac{1}{N}\sum_{n=1}^{N}\sum_{j=1}^{d} |R_{\text{mom},j}(x_n, t_n)|^2 \tag{27}$$

$$L_{\text{GE}} = \lambda_1 L_{\text{cont}} + \lambda_2 L_{\text{mom},j} \tag{28}$$

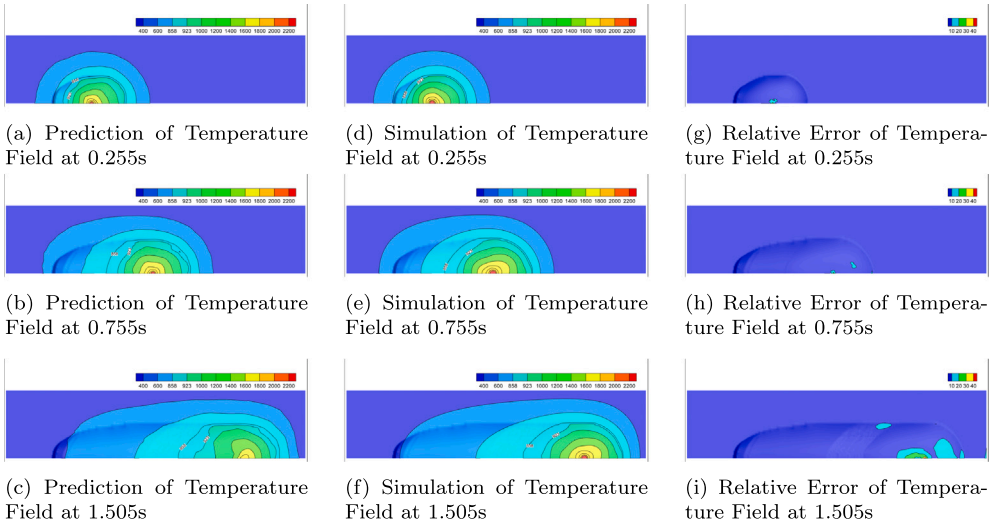

(a) Prediction of Temperature Field at 0.255s
(d) Simulation of Temperature Field at 0.255s
(g) Relative Error of Temperature Field at 0.255s
(b) Prediction of Temperature Field at 0.755s
(e) Simulation of Temperature Field at 0.755s
(h) Relative Error of Temperature Field at 0.755s
(c) Prediction of Temperature Field at 1.505s
(f) Simulation of Temperature Field at 1.505s
(i) Relative Error of Temperature Field at 1.505s

Fig. 2. PCRF-Net vs simulation: temperature field comparison with error analysis.

4. Result

This section discusses the comparison between the laminar flow simulation model and PCRF-Net predictions at a scanning speed of $v = 18\,\text{mm/s}$ and power of 1000 W. All simulation data are obtained from a laminar flow finite volume solver, which is thoroughly compared with experimental data by Chen et al. [21].

Training data uses a coarse grid (148×34×41), and PCRF-Net extends the prediction results to a fine grid ($292 \times 66 \times 41$) through interpolation methods. It should be noted that interpolation is performed only in the x and y directions, while the z direction maintains the original resolution. This is because the z direction is the welding direction, where continuous material addition occurs during the welding process, leading to fundamental differences in the physical field distribution compared to the x and y directions. Therefore, interpolation is not suitable for this direction. Unless otherwise specified, all prediction results in this section are at fine grid ($292 \times 66 \times 41$) resolution and are compared with numerical simulation results at the same resolution. All simulation results are obtained under the aforementioned operating conditions.

Regarding computational time, the **first-time cost** includes: numerical simulation on the $148 \times 34 \times 41$ grid (17,073 s), TC-Branch training (2519 s), VF-Branch training (1725 s), and prediction, representing the complete workflow time. **After training** refers to the time required only for prediction after the model training is completed. For the same operating conditions, at grid resolution $292 \times 66 \times 41$, traditional numerical simulation requires 122,136 s, while the PCRF-Net method (first-time use) requires only 21,328 s, achieving an **acceleration of approximately 5.73 times**. The results demonstrate that PCRF-Net can effectively predict multi-physics field distributions under laminar flow conditions, and can complete predictions in seconds after training.

4.1. TC-branch temperature field prediction

Fig. 2 shows the comparison between PCRF-Net predicted temperature fields, numerical simulations, and relative errors at three time points ($t = 0.255, 0.755, 1.505\,\text{s}$) (top view). At $t = 1.505\,\text{s}$, the system has reached a stable convergence state, with the temperature field distribution tending to be stable. The relative error plots demonstrate that the majority of the domain exhibits low relative errors (below 10%).

Due to the limitations of the top view perspective, the complete three-dimensional boundary features of the molten pool cannot be fully displayed. Therefore, Table 5 uses numerical metrics (width, height, depth, and length of the molten pool) to quantitatively evaluate prediction accuracy. The table compares the maximum temperature and geometric metrics of the molten pool at steady state, including results from physical experiments, numerical simulations, and PCRF-Net predictions.

Table 5
Comparison of Molten Pool Geometries from experimental, numerical simulation, and PCRF-Net predictions.

Characteristics	Exp.	Sim. ($292 \times 66 \times 41$)	Pred. ($292 \times 66 \times 41$)
Length (mm)	17.5	14.572	14.866
Width (mm)	5.3	5.027	5.118
Height (mm)	1.7	1.223	1.458
Depth (mm)	1.2	1.933	0.652
Cost Time (s)[a]	–	122,136	21,327.54
Cost Time (s)[b]	–	–	10.54

[a] First-time cost (including simulation, training, and prediction);
[b] After training (prediction only).

Table 6
Generalization performance of PCRF-Net across different grid resolutions.

Grid Resolution	$I \times J \times K$	R^2	MSE	Cost Time (s)[a]
Training Grid	$148 \times 34 \times 41$	0.9976	1.00×10^{2}	0.67
Test Grid 1	$292 \times 34 \times 41$	0.9918	3.37×10^{2}	6.45
Test Grid 2	$292 \times 66 \times 41$	0.9703	1.36×10^{3}	10.54

[a] After training (prediction only). The model is trained on the coarse grid ($148 \times 34 \times 41$) as in Table 5.

To demonstrate the grid resolution generality of PCRF-Net, Table 6 evaluates the model's performance across different grid resolutions. The model is trained on the coarse grid ($148 \times 34 \times 41$) and tested on finer grids via interpolation.

4.2. TC-branch concentration field prediction

Fig. 3 shows the comparison between PCRF-Net predicted concentration fields, numerical simulations, and absolute errors at three time points ($t = 0.255, 0.755, 1.505\,\text{s}$) (front view). The absolute error plots demonstrate that the errors are generally low throughout the domain, with higher errors primarily localized at the boundaries of the concentration distribution.

To evaluate the generalization performance of PCRF-Net for concentration field prediction, Table 7 compares the model's performance across different grid resolutions.

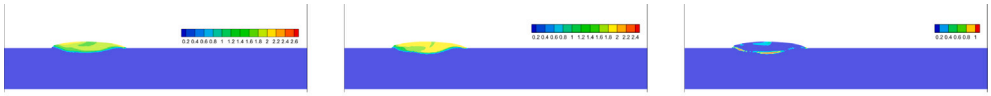

(a) Prediction of Concentration Field at 0.255s

(d) Simulation of Concentration Field at 0.255s

(g) Absolute Error of Concentration Field at 0.255s

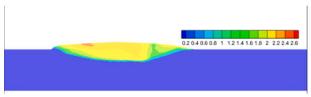

(b) Prediction of Concentration Field at 0.755s

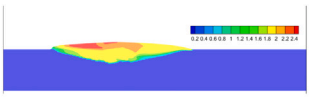

(e) Simulation of Concentration Field at 0.755s

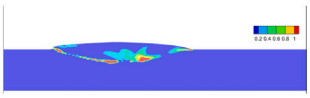

(h) Absolute Error of Concentration Field at 0.755s

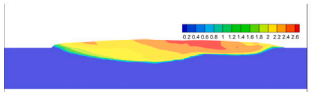

(c) Prediction of Concentration Field at 1.505s

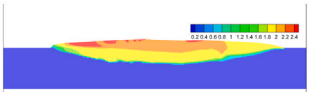

(f) Simulation of Concentration Field at 1.505s

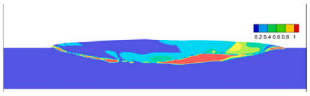

(i) Absolute Error of Concentration Field at 1.505s

Fig. 3. PCRF-Net vs Simulation: concentration field comparison with error analysis.

Table 7
Generalization performance of PCRF-Net for the concentration field across different grid resolutions.

Grid Resolution	$I \times J \times K$	R^2	MSE	Cost Time (s)[a]
Training Grid	$148 \times 34 \times 41$	0.9915	3.73×10^{-3}	0.67
Test Grid 1	$292 \times 34 \times 41$	-1.8722	1.88×10^{-1}	6.45
Test Grid 2	$292 \times 66 \times 41$	0.9028	4.30×10^{-2}	10.54

[a] After training (prediction only). The model is trained on the coarse grid ($148 \times 34 \times 41$) as shown in Table 5.

The model demonstrates good generalization performance on the training grid and the interpolated grid $292 \times 66 \times 41$, with R^2 values of 0.9915 and 0.9028, respectively. However, the performance degrades significantly on the interpolated grid $292 \times 34 \times 41$. This performance degradation is attributed to the highly anisotropic grid aspect ratio created by interpolating only in one direction, which leads to poor prediction accuracy. The concentration field, with its smaller value range compared to temperature, is more sensitive to interpolation-induced errors. This observation highlights the importance of balanced grid interpolation for accurate concentration field prediction.

4.3. Velocity field prediction

4.3.1. VF-branch velocity field prediction

Fig. 4 shows the comparison between PCRF-Net predicted velocity fields and simulations at three time points ($t = 0.255, 0.755, 1.505$ s). Arrows represent the direction of the combined u, v, and w components, and the arrow length indicates the magnitude of the velocity. At all time points, the predictions from PCRF-Net (left column) and numerical simulations (right column) show high consistency in trends in the molten pool boundary and heat-affected zone.

To evaluate the generalization performance of PCRF-Net for velocity field prediction, Table 8 compares the model's performance across

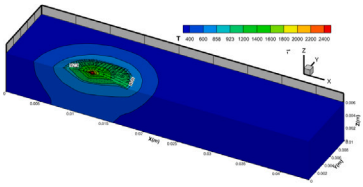

(a) PIML Prediction of Velocity Field at 0.255s

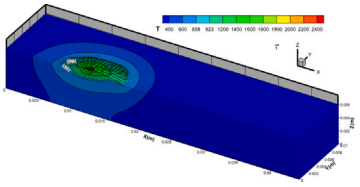

(d) Simulation of Velocity Field at 0.255s

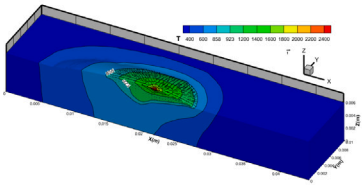

(b) PIML Prediction of Velocity Field at 0.755s

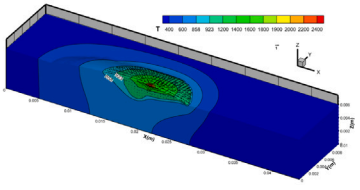

(e) Simulation of Velocity Field at 0.755s

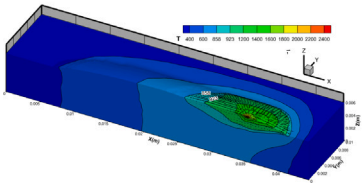

(c) PIML Prediction of Velocity Field at 1.505s

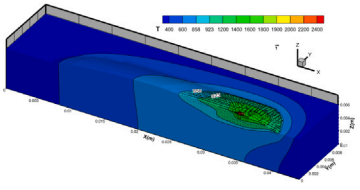

(f) Simulation of Velocity Field at 1.505s

Fig. 4. PIML vs Numerical Simulation: Velocity Field.

Table 8
Generalization Performance of PCRF-Net for velocity field across different grid resolutions.

Grid Resolution	$I \times J \times K$	R^2 (Pe)	Cost Time (s)[a]
Training Grid	$148 \times 34 \times 41$	0.9233	0.67
Test Grid 1	$292 \times 34 \times 41$	0.8695	6.45
Test Grid 2	$292 \times 66 \times 41$	0.8727	10.54

[a] After training (prediction only). The model is trained on the coarse grid ($148 \times 34 \times 41$) as in Table 5.

Table 9
Pe statistics for two architectures.

Metric	Architecture	Mean	Std	R^2	Improvement
Peclet Number Pe	Simulation	1443.60	2129.41	–	–
Peclet Number Pe	Standard PINN	1613.48	2667.77	0.8063	–
Peclet Number Pe	**VF-Branch**	**1438.63**	**2215.85**	**0.8727**	**+8.2%**

different grid resolutions. The evaluation uses the Peclet number (Pe) as a key metric. The Peclet number is defined as $Pe = \frac{UL}{D}$, where U is the characteristic velocity, L is the characteristic length, and D is the diffusion coefficient. It characterizes the relative importance of convection to diffusion and serves as an important dimensionless parameter for evaluating the accuracy of flow structure predictions.

The model demonstrates stable generalization performance across different grid resolutions, indicating good grid resolution generality of PCRF-Net for velocity field prediction.

4.3.2. Comparative results: VF-branch vs standard PINN

To verify the effectiveness of Fourier enhancement for velocity-field prediction, we conducted a comparative experiment between the Fourier-enhanced VF-Branch and the standard PINN. Both architectures used the same training strategy, loss functions, and hyperparameters; the only difference is whether frequency-domain features are extracted via the Fourier transform.

Table 9 reports the quantitative comparison for velocity-field prediction.

The results show that, over all zones, the Fourier-enhanced VF-Branch achieves an R^2 of 0.8727 for pointwise Peclet number predictions, compared to 0.8063 for the standard PINN (an 8.2% improvement). Its predicted Pe distribution is also closer to the simulation, indicating a better match to the simulated flow. This confirms the effectiveness of Fourier enhancement for velocity-field prediction.

4.3.3. Sensitivity analysis of Fourier mode count

To determine the optimal number of Fourier features, we conducted a systematic sensitivity analysis. We tested different numbers of Fourier modes (4, 8, 12, 16, 20, 24, 32), with each configuration using the same training strategy, loss function, and hyperparameter settings, with the only difference being the number of Fourier modes.

Table 10 presents the prediction performance comparison results for different numbers of Fourier modes. The evaluation is based on the full grid (292×66×41) data. Reference simulation values: velocity magnitude

Table 10
Sensitivity analysis of Fourier mode numbers.

Fourier Modes	$\lvert V\rvert$ R^2	$\lvert V\rvert$ Mean	$\lvert V\rvert$ Std	Pe R^2	Pe Mean	Pe Std
4	0.0402	0.1637	0.1118	0.0402	1403.12	958.28
8	0.6528	0.1309	0.1757	0.6528	1121.75	1505.83
12	0.7099	0.1951	0.3140	0.7099	1671.62	2690.86
16	0.5021	0.1166	0.1427	0.5021	998.95	1223.37
20	**0.8727**	**0.1679**	**0.2586**	**0.8727**	**1438.63**	**2215.85**
24	0.8670	0.1726	0.2696	0.8670	1479.10	2310.64
32	0.8249	0.1482	0.2089	0.8249	1270.20	1790.36

Table 11
Comparison between unified architecture and PCRF-Net.

Physical Field	Metric	Unified Architecture	PCRF-Net	Improvement
Temperature (T)	R^2	0.9845	0.9703	−1.4%
Concentration (C)	R^2	0.5097	0.9028	+77.1%
Velocity	R^2 (Pe)	0.1706	0.8727	+411.4%

$|V|$ has a mean of **0.1684** and a standard deviation of **0.2485**; Peclet number Pe has a mean of **1443.60** and a standard deviation of **2129.41**.

From the results, it can be observed that an insufficient number of modes leads to severe underfitting, while an excessive number of modes results in prediction accuracy slightly lower than the optimal value. Twenty Fourier modes achieve the highest prediction accuracy (R^2 = 0.8727) among all configurations, and the predicted mean and standard deviation of both velocity magnitude $|V|$ and Peclet number Pe are closest to the true values. Therefore, 20 modes are selected as the standard configuration for the VF-Branch.

4.4. Comparison with unified training architecture

To validate the effectiveness of the dual-branch architecture, we conducted a systematic comparison between PCRF-Net and the traditional unified training architecture. The baseline architecture employs a unified network structure that merges the network components of the dual-branch architecture (ResNet-MLP and Fourier-enhanced MLP) into a single network, simultaneously predicting all physical fields (T, C, u, v, w), with all physical quantities trained together using a unified loss function. The only difference between the two architectures lies in the training strategy: the dual-branch architecture adopts step-by-step training, while the baseline architecture employs unified training, where all physical fields are trained simultaneously.

Table 11 presents the quantitative comparison results of the two architectures across different physical fields. Training is based on the $148 \times 34 \times 41$ grid, and evaluation is based on the $292 \times 66 \times 41$ grid data.

The comparison results demonstrate that when the unified architecture trains all physical fields simultaneously, due to inconsistent training convergence characteristics, the velocity field almost fails to learn. PCRF-Net achieves significant improvements in concentration field prediction accuracy (R^2 increases from 0.5097 to 0.9028, an improvement of +77.1%), substantial improvements in velocity field prediction accuracy (Peclet number R^2 increases from 0.1706 to 0.8727, an improvement of +411.4%), while temperature field prediction accuracy slightly decreases but remains at a high level (R^2 = 0.9703).

5. Conclusion

This paper proposes a Physics-Informed Coupled Residual-Fourier Neural Network (PCRF-Net) for efficient multi-physics field prediction in the melt pool during hybrid laser-MIG welding. PCRF-Net employs a dual-branch architecture with stepwise training: the TC-Branch predicts temperature and concentration, while the VF-Branch predicts velocity components. The stepwise training strategy decouples the complex coupling between physical fields, improving training stability. Experimental results demonstrate high consistency with numerical simulations and significant computational efficiency improvements.

Although PCRF-Net demonstrates promising results, we acknowledge several limitations arising from simulation-only validation: (1) Simplified boundary conditions: The numerical simulation may not fully capture all complex factors in actual welding processes, such as environmental convection, radiation losses, and surface oxidation. (2) Material parameter accuracy: The simulation model relies on the accuracy of material parameters, which may vary with temperature, phase transitions, and other factors, potentially introducing uncertainties in practical applications. These limitations need to be further evaluated and improved through experimental validation.

Looking forward, the dual-branch decoupling strategy of PCRF-Net can be extended to other multi-physics coupling problems. Adopting different network architectures and stepwise training strategies for different physical fields based on their characteristics can effectively decouple complex multi-physics coupling, improving training stability and prediction efficiency. Future work can apply this decoupling approach to problems such as multiphase flow and coupled heat and mass transfer, providing new solutions for rapid prediction of complex engineering problems.

CRediT authorship contribution statement

Wenbo Zhou: Writing – original draft, Visualization, Validation, Software, Methodology, Formal analysis, Data curation. **Le Song:** Writing – review & editing, Writing – original draft, Validation, Supervision, Investigation. **Xuyang Chen:** Project administration, Methodology, Funding acquisition, Conceptualization. **Zhiyong Huang:** Writing – review & editing. **Baorui Du:** Writing – review & editing.

Declaration of competing interest

The authors declare that they have no known competing financial interests or personal relationships that could have appeared to influence the work reported in this paper.

Data availability

Data will be made available on request.

References

[1] N. Contuzzi, M. Rashkowets, G. Casalino, A methodology for multi-object optimization of laser/mig hybrid welding process, Procedia CIRP, in: 16th CIRP Conference on Intelligent Computation in Manufacturing Engineering, vol. 118, 2023, pp. 907–911, https://doi.org/10.1016/j.procir.2023.06.156, https://www.sciencedirect.com/science/article/pii/S2212827123003839.

[2] J. Wang, R. Zhu, Y. Liu, L. Zhang, Understanding melt pool characteristics in laser powder bed fusion: an overview of single- and multi-track melt pools for process optimization, Adv. Powder Mater. 2 (4) (2023) 100137, https://doi.org/10.1016/j.apmate.2023.100137, https://www.sciencedirect.com/science/article/pii/S2772834X23000295.

[3] P. Cook, A. Murphy, Simulation of melt pool behaviour during additive manufacturing: underlying physics and progress, Addit. Manuf. (2019) 100909, https://doi.org/10.1016/j.addma.2019.100909

[4] A. Kumar, T. Debroy, Heat transfer and fluid flow during gas-metal-arc fillet welding for various joint configurations and welding positions, Metall. Mater. Trans. A 38 (2007) 506–519, https://doi.org/10.1007/s11661-006-9083-4

[5] A. Anca, A. Cardona, J. Risso, V.D. Fachinotti, Finite element modeling of welding processes, Appl. Math. Model. 35 (2) (2011) 688–707, https://doi.org/10.1016/j.apm.2010.07.026, https://www.sciencedirect.com/science/article/pii/S0307904X10002751.

[6] J. Zhou, H.L. Tsai, Modeling of transport phenomena in hybrid laser-mig keyhole welding, Int. J. Heat Mass Transf. 51 (17) (2008) 4353–4366, https://doi.org/10.1016/j.ijheatmasstransfer.2008.02.011, https://www.sciencedirect.com/science/article/pii/S0017931008001099.

[7] P. Jiang, S. Gao, S. Geng, C. Han, G. Mi, Multi-physics multi-scale simulation of the solidification process in the molten pool during laser welding of aluminum alloys, Int. J. Heat Mass Transf. 161 (2020) 120316, https://doi.org/10.1016/j.ijheatmasstransfer.2020.120316, https://www.sciencedirect.com/science/article/pii/S001793102033252X.

[8] Q. Xia, G. Sun, J. Kim, Y. Li, Multi-scale modeling and simulation of additive manufacturing based on fused deposition technique, Phys. Fluids 35 (3) (2023) 034116, https://doi.org/10.1063/5.0141316, https://pubs.aip.org/aip/pof/article-pdf/doi/10.1063/5.0141316/19825917/034116_1_online.pdf.

[9] Q. Zhu, Z. Lu, Y. Hu, Transfer learning-enhanced physics informed neural network for accurate melt pool prediction in laser melting, Adv. Manuf. 2 (1) (2025), https://doi.org/10.55092/am20250001

[10] S. Guo, M. Agarwal, C. Cooper, Q. Tian, R.X. Gao, W. Guo, Y.B. Guo, Machine learning for metal additive manufacturing: towards a physics-informed data-driven paradigm, J. Manuf. Syst. 62 (2022) 145–163, https://doi.org/10.1016/j.jmsy.2021.11.003, https://www.sciencedirect.com/science/article/pii/S0278612521002259.

[11] S. Koric, D.W. Abueidda, Data-driven and physics-informed deep learning operators for solution of heat conduction equation with parametric heat source, Int. J. Heat Mass Transf. 203 (2023) 123809, https://doi.org/10.1016/j.ijheatmasstransfer.2022.123809, https://www.sciencedirect.com/science/article/pii/S0017931022012777.

[12] S. Li, G. Wang, Y. Di, L. Wang, H. Wang, Q. Zhou, A physics-informed neural network framework to predict 3D temperature field without labeled data in process of laser metal deposition, Eng. Appl. Artif. Intell. 120 (2023) 105908, https://doi.org/10.1016/j.engappai.2023.105908, https://www.sciencedirect.com/science/article/pii/S0952197623000921.

[13] H. Wang, B. Li, F.-Z. Xuan, A dimensionally augmented and physics-informed machine learning for quality prediction of additively manufactured high-entropy alloy, J. Mater. Process. Technol. 307 (2022) 117637, https://doi.org/10.1016/j.jmatprotec.2022.117637, https://www.sciencedirect.com/science/article/pii/S0924013622001492.

[14] P. Akbari, F. Ogoke, N.-Y. Kao, K. Meidani, C.-Y. Yeh, W. Lee, A. Barati Farimani, Meltpoolnet: melt pool characteristic prediction in metal additive manufacturing using machine learning, Addit. Manuf. 55 (2022) 102817, https://doi.org/10.1016/j.addma.2022.102817, https://www.sciencedirect.com/science/article/pii/S2214860422002172.

[15] M. Bayat, W. Dong, J. Thorborg, A.C. To, J.H. Hattel, A review of multi-scale and multi-physics simulations of metal additive manufacturing processes with focus on modeling strategies, Addit. Manuf. 47 (2021) 102278, https://doi.org/10.1016/j.addma.2021.102278, https://www.sciencedirect.com/science/article/pii/S2214860421004383.

[16] R. Sun, H. Jeong, J. Zhao, Y. Gou, E. Sauret, Z. Li, Y. Gu, A physics-informed neural network framework for multi-physics coupling microfluidic problems, Comput. Fluids 284 (2024) 106421, https://doi.org/10.1016/j.compfluid.2024.106421, https://www.sciencedirect.com/science/article/pii/S0045793024002524.

[17] S. Plankovskyy, Y. Tsegelnyk, N. Shyshko, I. Litvinchev, T. Romanova, J.M. Velarde Cantú, Review of physics-informed neural networks: challenges in loss function design and geometric integration, Mathematics 13 (20) (2025), https://doi.org/10.3390/math13203289, https://www.mdpi.com/2227-7390/13/20/3289.

[18] J. Peng, L. Li, S. Lin, F. Zhang, Q. Pan, S. Katayama, High-speed x-ray transmission and numerical study of melt flows inside the molten pool during laser welding of aluminum alloy, Math. Probl. Eng. 2016 (1) (2016) 1409872, https://doi.org/10.1155/2016/1409872, https://onlinelibrary.wiley.com/doi/pdf/10.1155/2016/1409872.

[19] L. Zhang, X. Li, Z. Nie, H. Huang, J. Sun, Softening behavior of a new Al-Zn-Mg-Cu alloy due to tig welding, J. Mater. Eng. Perform. 25 (2016) 1870–1879.

[20] H.L. Wei, J.W. Elmer, T. DebRoy, Origin of grain orientation during solidification of an aluminum alloy, Acta Mater. 115 (2016) 123–131.

[21] X. Chen, G. Yu, X. He, S. Li, Z. Li, Numerical study of heat transfer and solute distribution in hybrid laser-mig welding, Int. J. Therm. Sci. 149 (2020).

[22] Z.H. Rao, S.M. Liao, H.L. Tsai, Modelling of hybrid laser–gma welding: review and challenges, Sci. Technol. Weld. Join. 16 (2013) 300–305.

[23] H.L. Wei, J. Mazumder, T. DebRoy, Evolution of solidification texture during additive manufacturing, Sci. Rep. 5 (2015) 16446.

[24] Y. Hu, X. He, G. Yu, Z. Ge, C. Zheng, W. Ning, Heat and mass transfer in laser dissimilar welding of stainless steel and nickel, Appl. Surf. Sci. 258 (15) (2012) 5914–5922, https://doi.org/10.1016/j.apsusc.2012.02.143, https://www.sciencedirect.com/science/article/pii/S0169433212003996.